ORIGINAL ARTICLE

Cytometry PART A
Journal of the International Society for Advancement of Cytometry

# Texture-Based Segmentation and a New Cell Shape Index for Quantitative Analysis of Cell Spreading in AFM Images

**Volkan Müjdat Tiryaki,[1]* Usienemnfon Adia-Nimuwa,[2] Virginia M. Ayres,[2] Ijaz Ahmed,[3] David I. Shreiber[3]**

[1]Department of Computer Engineering, Siirt University, Siirt, 56100, Turkey

[2]Department of Electrical and Computer Engineering, Michigan State University, East Lansing, Michigan, 48824

[3]Department of Biomedical Engineering, Rutgers, The State University of New Jersey, Piscataway, New Jersey, 08854

Grant sponsor: National Science Foundation, Grant numbers: PHY-0957776; ARRA-CBET-0846328

Grant sponsor: the General Directorate of High Education, Ministry of National Education of the Republic of Turkey.

Additional Supporting Information may be found in the online version of this article.

Correspondence to: Volkan Müjdat Tiryaki, College of Engineering and Architecture, Block B, Siirt University, Kezer Campus, Siirt 56100, Turkey.
E-mail: tiryakiv@siirt.edu.tr

Published online 2 November 2015 in Wiley Online Library (wileyonlinelibrary.com)

DOI: 10.1002/cyto.a.22739



## Abstract

A new cell shape index is defined for use with atomic force microscopy height images of cell cultures. The new cell shape index reveals quantitative cell spreading information not included in a conventional cell shape index. A supervised learning-based cell segmentation algorithm was implemented by texture feature extraction and a multi-layer neural network classifier. The texture feature sets for four different culture surfaces were determined from the gray level co-occurrence matrix and local statistics texture models using two feature selection algorithms and by considering computational cost. The quantitative morphometry of quiescent-like and reactive-like cerebral cortical astrocytes cultured on four different culture environments was investigated using the new and conventional cell shape index. Inclusion of cell spreading with stellation information through use of the new cell shape index was shown to change biomedical conclusions derived from conventional cell shape analysis based on stellation alone. The new CSI results showed that the quantitative astrocyte spreading and stellation behavior was induced by both the underlying substrate and the immunoreactivity of the astrocytes. 

## Key terms

cell spreading; stellation; immunoreactivity; texture-based cell segmentation; floating feature selection; cell–material interactions

A cell shape index (CSI) is a dimensionless quantitative measure of cell morphology acquired from images. Cells have different morphologies depending on their type in vivo, e.g., astrocytes have a stellate morphology in the central nervous system (CNS) for interactions with neurons and capillaries (1), while endothelial cells in heart arteries have an elongated morphology with actin and microtubule fibers aligned parallel to the direction of blood flow (2). *In vitro*, cells also adopt distinctive morphologies that approximately recapitulate their in vivo counterparts and that can be influenced by a controlled environment. Quantitative cell morphology investigations have recently been used to explore the potentially significant directive impact of environments for healthy or pathological cellular outcomes (3–7).

A conventional CSI in widespread use is the ratio of perimeter squared to the cell projection area (1):

$$\mathrm{CSI} = \frac{P^2}{4\pi A} \tag{1}$$

where $P$ is cell perimeter and $A$ is cell projection area. This equation describes stellation as a cell's departure from a circular projection since:

$$\frac{(2\pi r)^2}{4\pi(\pi r^2)} = 1 \quad (2)$$

The conventional CSI has been previously used to evaluate morphology of astrocytes (1) and vascular endothelial cells (2). However, this definition for CSI, which was created for use with two-dimensional (2D) optical microscopy images, does not include three-dimensional (3D) effects, e.g., cell-spreading or hypotonic swelling.

New research directions are actively being pursued to enhance the usefulness of cell shape analysis in biomedical research. Two important directions are research to incorporate and analyze 3D information and research to segment cells for CSI analysis. Addressing the former, Canham and Burton have proposed a "sphericity index" for the study of human red blood cells (8). Their volumetric CSI is highly appropriate for optical microscopy images of blood cells in a 3D environment. The 2D and 3D discrete compactness measures that are invariant under translation, rotation, and scaling were developed by Bribiesca (9). Chvátal et al. have recently developed a 3D cell morphometry definition for use with z-series confocal microscopy images (10). A 3D model retrieval that uses both semantic concepts and 2D and 3D classical compactness measures shape indexes was proposed by Kassimi et al. (11). The 2D shape indexes and texture features measured from cell nuclei were recently used to classify healthy and pathological skin fibroblast by Thibault et al. (12). Farooque et al. (13) have recently proposed a dimensionality matrix to assess gyration tensor ellipsoids that are fit to each cell, and then classified the ellipsoids as 1D, 2D, or 3D. The $L_1^{0.5}/L_3^{0.5}$ measure in Ref. 13 can be used to quantitatively estimate the cell spreading behavior for cell types and/or biological events that are dominated by the cell soma response, e.g., hypotonic swelling. For other cell types such as neurons and astrocytes, the cell process extension response is equally important. This adds an additional level of complexity as the process volumes must be included with the cell soma result.

Addressing the latter, CSI analysis is a revealing but currently under-utilized approach because CSI calculation requires a clearly defined cell perimeter, which is a segmentation issue. Automatic extraction of cell boundary information using, e.g., NIH Image J 1.46r is limited to isolated cells with perimeters that display sharp contrast. In recent work by Pincus and Theriot (14), a mask and template matching approach was innovatively applied to confluent cells in culture to create an accurate numerical 2D representation for individual cells with extractable boundaries. Tiryaki et al. developed a new CSI that incorporates volumetric information acquired from high-resolution AFM height images of cell-scaffold/substrates interactions (15). This utilized a Gaussian high-pass filter (GHPF) design followed by histogram equalization that enabled the edges and processes to be clearly distinguished; however, the final cell boundaries were determined by manual segmentation. In the present investigation, a new cell segmentation approach that is based on supervised learning and texture analysis is developed to semiautomatically extract cell–substrate boundaries with minimum user bias, which greatly facilitates use of the new AFM-based CSI.

AFM is becoming increasingly important for biomedical research as it provides direct high-resolution information with minimal sample preparation. Recent AFM-based biomedical investigations include studies of multi-scale nano-mechanical hierarchies present within hydrogel intermediate filament phantoms (16), multi-scale nano-mechanical assembly present during tendon embryogenesis (17), cytoskeletal rounding during mitosis (18), and myosin walking with head torsion (19). In the present work, we present investigations using the new volumetric CSI definition based on analysis of high-resolution AFM images (15) that incorporates the new semi-automatic texture-based cell segmentation analysis. AFM height images retain volumetric information for both cell spreading and cell processes, making the new CSI appropriate for investigations of all substrate-adherent cell cultures and surface seeding of 3D matrix cultures.

In the present investigation, the new AFM-based CSI is used to quantitatively analyze the responses of quiescent-like and reactive-like (dibutyryl cyclic adenosine monophosphate (dBcAMP)-treated) astrocytes to the nanophysical cues provided by four culture environments including a biomimetic polyamide nanofibrillar scaffold environment. Astrocyte reactivity induced by dBcAMP-treatment recapitulates elements of CNS traumatic injury. We are especially interested in astrocyte responses to polyamide nanofibrillar scaffolds, as these appear to favorably modulate the glial scar response that blocks axon regeneration in CNS traumatic injury (20,21). Our previous AFM studies determined that significant responses include cell spreading as well as process formation, and that the cell spreading can vary, depending on the surface polarity of the cell environment (3). In the present work, we use the new CSI to perform a quantitative 3D cell spreading and stellation response investigation of astrocytes in response to (1) changes in nanophysical environment cues and (2) dBcAMP-treatment.

## Materials and Methods

### Nanofibrillar Scaffolds and Comparative Culture Surfaces

Four cell culture surfaces were investigated: poly-L-lysine-functionalized planar glass (PLL glass), unfunctionalized planar Aclar (Aclar), PLL-functionalized planar Aclar (PLL Aclar), and polyamide nanofibrillar scaffolds. Glass coverslips (12 mm, No. 1 coverglass, Fisher Scientific, Pittsburgh, PA) and Aclar coverslips (12 mm, Ted Pella, Redding, CA) were used as underlying surfaces for the PLL functionalization. Glass or Aclar coverslips were placed in a 24-well tissue culture plate (one coverslip/well) and covered with 1 mL of poly-L-lysine (PLL) solution (50 $\mu$g PLL mL$^{-1}$ in $dH_2O$) overnight. The coverslips used for the cultures were then rinsed with $dH_2O$ and sterilized with 254 nm UV light using a Spectronics Spectrolinker XL-1500 (Spectroline Corporation, Westbury, NY). The polyamide nanofibrillar scaffolds electrospun on Aclar substrates were obtained from Donaldson (Minneapolis,

MN) and Corning Life Sciences (Lowell, MA). The fiber diameter for the nanofibrillar scaffolds has a range from ~100 to ~300 nm.

Promising in vivo and in vitro results have been obtained for astrocytes in contact with these nanofibrillar scaffolds, as implants or as culture surfaces. In our recent work (3,4), astrocyte responses to the nanofibrillar scaffolds were studied in comparison with their responses to three additional culture surfaces: PLL glass, Aclar, and PLL Aclar. PLL glass is a standard astrocyte culture surface, and astrocyte responses to it are well characterized, making it useful for identifying differences in astrocyte responses to other surfaces. The polyamide nanofibrillar scaffolds were electrospun on Aclar substrates. Astrocyte responses to PLL Aclar surfaces were studied to clarify the role of the underlying substrate versus surface functionalization.

### Primary Quiescent-like and Reactive-like Astrocyte Cultures

Primary quiescent-like astrocyte cultures were prepared from new born Sprague Dawley (postnatal Day 1 or 2) rats (3). All procedures were approved by the Rutgers Animal Care and Facilities Committee (IACUC Protocol #02-004). The rat pups were sacrificed by decapitation and the cerebral hemispheres were isolated aseptically. The cerebral cortices were dissected out, freed of meninges, and collected in Hank's buffered saline solution (HBSS; Mediatech, Herndon, VA). The cerebral cortices were then minced with sterile scissors and digested in 0.1% trypsin and 0.02% DNase for 20 min at 37°C. The softened tissue clumps were then triturated by passing several times through a fine bore glass pipette to obtain a cell suspension. The cell suspension was washed twice with culture medium [Dulbecco's Modified Eagle's Medium (DMEM; Life Technologies, Carlsbad, CA) +10% fetal bovine serum (FBS, Life Technologies)] and filtered through a 40-$\mu$m nylon mesh. For culturing, the cell suspension was placed in 75-cm$^2$ flasks (one brain/flask in 10 mL growth medium) and incubated at 37°C in a humidified $CO_2$ incubator. After 3 days of incubation, the growth media was removed, cell debris was washed off, and fresh medium was added. The medium was changed every 3–4 days. After reaching confluency (~7 days), the cultures were shaken to remove macrophages and other loosely adherent cells.

To obtain reactive-like astrocytes, 0.25 mM dibutyryl cyclic adenosine monophosphate (dBcAMP) was added to the culture medium of 7-day-old semi-confluent quiescent astrocyte cultures and the serum concentration was reduced to 1%. The cultures in dBcAMP containing medium were incubated for additional 7–8 days with a media change every 3–4 days. The morphology of the cells was observed on alternate days under a phase contrast microscope. In the control cultures, the cells were fed with DMEM + 1% FBS (without dBcAMP).

Quiescent-like and reactive-like astrocytes were harvested at the same time point using 0.25% Trypsin/ethylene-diaminetetraacetic acid (EDTA, Sigma-Aldrich, St. Louis, MO) and re-seeded at a density of 30,000 cells per well directly on 12-mm Aclar or PLL Aclar coverslips, PLL glass coverslips, or on Aclar coverslips coated with nanofibers in 24-well plates in astrocyte medium containing dBcAMP (0.5 mL). After culturing the astrocytes on the aforementioned substrates for 24 h, they were fixed with 4% paraformaldehyde for 10 min. Parallel cultures were immunostained with GFAP, an identification marker for astrocytes, and >95% were found to be GFAP-positive.

For atomic force microscopy investigation, the astrocytes cultured on coverslips were fixed in 4% paraformaldehyde for 10 min, rinsed with distilled water, and air-dried, but were not immunostained.

### AFM Imaging

AFM investigations were performed using a Nanoscope IIIa (Bruker AXS, Madison WI, formerly Veeco Metrology) operated in contact mode and in ambient air. A J scanner with 125 $\mu$m × 125 $\mu$m × 5.548 $\mu$m x-y-z scan range, and Bruker DNP silicon nitride probes with a 35° ± 2° cone angle, and a nominal 20-nm tip radius of curvature were used for AFM investigations. Cell segmentation for both the conventional and new CSI calculations was implemented with MATLAB version 7.7.0 (R2012b) (The MathWorks, Natick, MA) using the neural network and image processing toolboxes. For each culture surface and immunoreactivity group at least 50 astrocyte images were captured from different regions of at least three different cell substrates. AFM height and deflection images were 512 × 512 or 256 × 256 pixels with 8 bit gray level depth. The field of view of the images was 100 $\mu$m × 100 $\mu$m. AFM height images were stitched manually when a single astrocyte was in multiple AFM images.

The base level for all culture surfaces was determined by taking the average of substrate/scaffold region height values in the AFM height image. The pixel intensities of the astrocytes on nanofibrillar scaffolds were not always higher than the base level. Therefore, for the nanofibrillar scaffold cultures the cell region was divided into two regions: cell surface that is higher and lower than the base level. For the pixels that are higher than the base level, the cell volume was calculated according to the base level. When the astrocyte surface pixel intensities were lower than the base level, the thickness of the cell region was set to average astrocyte process thickness. Fifty AFM cross-section measurements, typically midway between the cell soma and the process end, were performed to determine the astrocyte process thickness, with results 193.2 ± 20.9 nm (mean ± SE) for quiescent-like astrocytes and 154.6 ± 20.1 nm (mean ± SE) for reactive-like astrocytes.

### Cell Segmentation of AFM Cell Culture Images

A supervised texture-based cell segmentation method was developed by extracting texture features from both AFM deflection and height images. We briefly explain the nature of these imaging modalities. In contact mode AFM (22,23), a probe attached to the end of a cantilever is scanned over the sample surface while the magnitude of cantilever deflection is measured from the reflected laser beam by a photodiode detector. A feedback loop maintains constant deflection via the input from the photodiode detector by applying a voltage to a piezoelectric actuator, which is capable of moving the

sample stage in the x-y-z direction at high resolution. The constant deflection means a constant force is applied to the sample by the cantilever. AFM height data is constructed by recording the voltage applied to the z piezo at the same time the probe's (x, y) position. The deflection data is obtained by recording the cantilever deflection that occurs prior to re-establishing the constant force. Therefore, an AFM deflection image is the height intensity differences between consecutive pixels, and hence mathematically the first-order derivative of the height image along the fast scan axis. This was tested by taking the first derivative of AFM height images using [1, −1] and "conv2" command in MATLAB, and confirming the correspondence of the deflection image captured by the instrument and the derivative of height image.

For cell segmentation, AFM raw data were exported as an ASCII file and AFM height and deflection images were loaded. To eliminate the nonlinearity from piezo scanners in the AFM height images, the images were flattened by subtracting a correction plane from the height image. The nonlinearity in the height images was in the vertical direction (slow scan axis). The correction plane was constructed by searching the column that has the minimum standard deviation, using a least-squares fit of that column to a second degree polynomial, and assuming each column has the same nonlinearity effect. The flattening step is different from the "flatten" command in the Nanoscope IIIa software and the step was implemented using "lsqcurvefit" command in MATLAB.

Sequential forward selection (SFS) and sequential forward floating selection (SFFS) (24) feature selection algorithms were used to identify the most discriminative features, avoid the effects of curse of dimensionality (25), and reduce the computational cost for cell segmentation. SFS and SFFS were implemented to determine the sub-optimal feature set from a total of 27 types of textural features including local statistics and GLCM texture feature models. The texture features were extracted from each pixel of AFM height and deflection images by setting the moving window size to 3 × 3, 5 × 5, and 7 × 7 determined by the minimal time required to classify culture surface and cell membrane texture patterns. The total time required for SFS calculation of PLL glass, Aclar, PLL Aclar, and nanofibrillar scaffolds using 5 × 5 mask size were 9 h 25 min, 5 h 48 min, 13 h 52 min, and 18 h 56 min, respectively.

Local statistics were used to estimate textures related to first, second, and higher order statistics. Standard deviation and mean by standard deviation features were defined as:

$$f_1=\sqrt{\frac{1}{N}\sum_{i=1}^{N}(p_i-\mu)^2} \tag{3}$$

$$f_2=\mu\sqrt{\frac{1}{N}\sum_{i=1}^{N}(p_i-\mu)^2} \tag{4}$$

where $\mu=\frac{1}{N}(p_1+\ldots+p_N)$, $p_i$ is the pixel intensity, and $N$ is the number of pixels in the moving window.

GHPF textural feature was calculated as described before (26). Texture measure A was defined as:

$$f_3=\sqrt{C_h(x,y)^2+C_v(x,y)^2} \tag{5}$$

where $C_h(x,y)=I*B$, * represents 2D convolution, $C_h$ and $C_v$ are the horizontal and vertical convolution, $I$ is input AFM image, and $B$ is a bar mask of the form [−1 2 −1] or [−1 −1 2 2–1 −1] (27).

Entropy is a measure of the uncertainty of a random variable (28), and was calculated by:

$$f_4=-\sum_{k=1}^{K}P[X=k]\log\left(P[X=k]\right) \tag{6}$$

where $X$ is the discrete random variable with $S_x=\{1,2,\ldots,K\}$ and $pmf\ \ p_k=P[X=k]$.

Skewness is a measure of symmetry and kurtosis is a measure of whether the data are peaked or flat relative to a normal distribution. These features were calculated as follows:

$$f_5=\frac{\sum_{i=1}^{N}(p_i-\mu)^3/N}{\sigma^3} \tag{7}$$

$$f_6=\frac{\sum_{i=1}^{N}(p_i-\mu)^4/N}{\sigma^4} \tag{8}$$

where $\mu$ and $\sigma$ are the means and standard deviations of the pixel intensities in the moving window.

Power spectrum of GHPF was more discriminative than the power spectrum of height images, and it was calculated from GHPF images by:

$$F(u,v)=\sum_{x=0}^{w-1}\sum_{y=0}^{h-1}G(x,y)e^{-2\pi i\left(\frac{ux}{w}+\frac{vy}{h}\right)} \tag{9}$$

$$f_7=|F(u,v)|^2 \tag{10}$$

where $G(x, y)$ is the GHPF image, and $F(u, v)$ is the discrete Fourier transform, which was calculated by using "fft2" command in MATLAB (29).

Local binary pattern (LBP), proposed in 1994 (30), is a type of feature which was shown to be useful for texture analysis and face recognition, and was defined as:

$$LBP=\sum_{i=0}^{N-1}u(t_i-t_c)2^i \tag{11}$$

where $u(x) = 1$ if $x \geq 0$ and $u(x) = 0$ otherwise. $N$ is the number of pixels in the moving window, $t_i$ is the intensity of neighboring pixel $i$, and $t_c$ is the intensity of the center pixel in the moving window. Moving window size was constant and 3. The rotational invariant version of LBP was calculated as (31):

$$f_8=LBP^{ri}=\min\{ROR(LBP,i)\ |\ i=0,1,\ldots,7\} \tag{12}$$

where $ROR(x, i)$ performs a circular bit-wise shift on the 8 bit number $x$ $i$ times until a maximal number of the most significant bits is 0.

Gray level co-occurrence matrix (GLCM) is a statistical method of extracting texture features from images (32).

GLCM texture features including contrast, correlation, energy, inverse difference moment, sum average, sum variance, sum entropy, entropy, difference variance, difference entropy, and information measures of correlation 1 and 2 were described and formulated by Haralick et al. (32). GLCM texture feature extraction was performed using fast calculation of Haralick's texture features (33). A total of 18 different types of GLCM features were calculated using equations given in the Supporting Information section.

The texture feature selection for cell segmentation is critical since it affects cell perimeter and cell area calculations, and hence the conventional and new CSI results. In SFS and SFFS algorithms, the newly found best texture feature was added to the current feature set when inclusion of the new feature resulted in at least 0.5% improvement in the cell segmentation recognition rate. Cell segmentation performance evaluation was based on the correctly classified pixels that belong to cell and substrate surface, and recognition rate was defined as:

$$\text{Recognition rate} = \frac{\text{TP}+\text{TN}}{\text{TP}+\text{TN}+\text{FP}+\text{FN}} \tag{13}$$

where TP, TN, FP, and FN denote true positive, true negative, false positive, and false negative, respectively. TP is the number of correctly classified cell pixels, TN is the number of correctly classified substrate/scaffold pixels, FP is the number of scaffold/substrate pixels that are incorrectly classified as cell pixels, and FN is the number of cell pixels that are incorrectly classified as scaffold/substrate pixels.

Neural networks were recently shown to have superior performance in image classification and segmentation (34,35). In the present work, an artificial neural network classifier was used to form the decision boundary for pixel-by-pixel classification of AFM cell culture images. The neural network has an input layer, two hidden layers, and an output layer. The activation functions of the first and second hidden layer were hyperbolic tangent and logarithmic sigmoid transfer function, respectively. The training of the neural network is performed by determining weights by resilient backpropagation algorithm (36). The average number of cell and scaffold/substrate surface training pixels was ~42,000 and 60,000, respectively. The number of weights was ~10% of the number of training patterns (37). The number of training iteration was determined empirically and set to 30 times the number of input features to avoid the overtraining of the classifier. The output layer of the neural network has two nodes that are trained to take [1 −1] when the output is cell pixel, and [−1 1] when the output is scaffold/substrate pixel. This is done to increase the performance of the neural network (37). Both nodes of the output layer are fed by the nodes in the second hidden layer. The number of nodes in the second hidden layer is 60. Let $n_4^j$ denote the output layer, then

$$n_4^j = \sum_{i=1}^{60} w_{34}^{i,j} n_3^i \text{ and } j=1,2 \tag{14}$$

where $n_3^i$ is the value of ith node of the second hidden layer, $w_{34}^{i,j}$ denote the weights between $n_3^i$ and $n_4^j$. The neural network is used to classify each AFM image pixel either as a "cell pixel" or a "substrate pixel," and the final classification method becomes the whole artificial neural network. The implementation of the neural network was performed using "newff" command in MATLAB. The cell versus substrate surface ground truth images were determined by observation for the Aclar, PLL Aclar, and PLL glass cell culture images. As reported in (26), cell boundaries on nanofibrillar scaffolds, are not easily distinguishable by human observation of either AFM height or deflection images. The cell and nanofibrillar scaffolds ground truth data were therefore determined using AFM GHPF cell culture images (26).

After the texture feature set was determined for each culture surface by SFS, SFSS algorithm, and human observation, texture features in the set were extracted, binarized, concatenated, and applied to the input of the classifier for training. The trained neural networks were saved, and the binary cell masks were obtained using the AFM images and trained networks. The morphological close operation and image filling were used to reduce the segmentation error. Small regions in the segmented images that were <1% of the whole image were eliminated, and then cell masks were ready for CSI and new CSI calculations.

### Astrocyte Morphology Investigation by New AFM-based CSI

The new CSI that includes volumetric information extracted from AFM images of cells on surfaces is defined as (15):

$$\text{New CSI} = \frac{\text{SA}_{\text{cell}}^3}{60.75\pi V_{\text{cell}}^2} \tag{15}$$

where $\text{SA}_{\text{cell}}$ is cell surface area and $V_{\text{cell}}$ is cell volume. The new CSI increases from 1 to $+\infty$ as cell becomes more stellate and/or the cell spreading increases. The assumptions, consistent with experiments, are that the cell is resting on, not penetrating, a surface, and that the cell is not fragmented. For a hemispherical "cell" on a surface, the new CSI is:

$$\frac{(0.5(4\pi r^2)+\pi r^2)^3}{60.75\pi\left(0.5\left({}^4/_3\pi r^3\right)\right)^2} = 1 \tag{16}$$

Departure from unity reflects the average departure from a 3D hemispherical volume by both stellation and cell spreading. The surface area of each cell was calculated by splitting the AFM topography faces into triangles. The area of a triangle in 3D space was computed using the cross product given by (38):

$$\text{SA}_{\text{triangle}} = 0.5\ |(v_2 - v_1) \times (v_3 - v_1)| \tag{17}$$

where $\text{SA}_{\text{triangle}}$ is area of a triangle on the cell surface and coordinates of the vertices are given by $vi = (xi, yi, zi)$. The surface area of each triangle was computed over the segmented cell area and then cell surface area was obtained. The volume of each astrocyte was calculated by assuming each pixel and its z coordinate as a square prism (39). The volume under each pixel was computed by multiplying the unit pixel

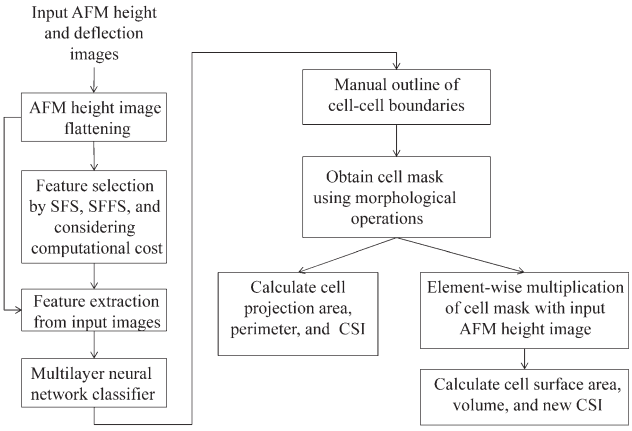


**Figure 1.** Flow chart of conventional and new CSI calculations.

area by the height of that pixel. This was repeated for all of the cell region pixels. The base level for all culture surfaces was determined by taking the average of substrate/scaffold height values in the AFM height image. Variations in the new CSI data among the culture surfaces were analyzed using ANOVA followed by pairwise post hoc comparisons with Tukey's test. Significance levels were set at $P < 0.05$.

### Astrocyte Morphology Investigation by Conventional CSI and Comparison

The conventional CSI definition given in Eq. (1) was used for comparison investigation of the quantitative morphometry of the cerebral cortical astrocytes cultured on the four different culture surfaces that presented different nanophysical cues (3). Variations in conventional CSI data among the culture surfaces were analyzed using ANOVA followed by pairwise post hoc comparisons with Tukey's test. Significance levels were set at $P < 0.05$. The illustration of conventional and new CSI calculation steps is shown in Figure 1.

## Results

### Cell Segmentation

**Strategy.** The individual recognition rates of each textural feature for the four culture surfaces, defined as the recognition rate [Eq. (13)] rendered as a percent, are shown in Figure 2. The highest recognition rates were observed for PLL glass because of its relatively smooth surface compared to cell surface. All GLCM features except dissimilarity, inertia, cluster shade, and cluster prominence were highly discriminative for cell segmentation on PLL glass. For nanofibrillar scaffolds and Aclar surfaces, the power spectrum and standard deviation were the most discriminative features, respectively. The lowest recognition rates were observed for the cell segmentation on PLL Aclar. The most discriminative feature for cell segmentation on PLL Aclar was mean by standard deviation. Power spectrum and standard deviation features were good discriminators on nanofibrillar scaffolds, Aclar, and PLL Aclar, while the recognition rates of $LBP^{ri}$ and GLCM features: dissimilarity, inertia, cluster shade, and cluster prominence were low for all culture surfaces.

The sub-optimal textural feature set for each culture surface found by SFS and SFFS algorithms is given in Table 1. In general, features extracted from height images were more discriminative than deflection images.

The cell segmentation performance depended on the window size as well as the culture surface and the texture features identified in the feature set found by feature selection algorithms. Three different window sizes were investigated in this work: $3 \times 3$, $5 \times 5$, and $7 \times 7$. The recognition rates increased as the window size was increased from $3 \times 3$ to $7 \times 7$ for all culture surfaces. The number of input texture feature (dimension) changed from one to four.

**Computational demand.** The decision for determining the final window size and feature set for cell segmentation was made by considering both the recognition rate and the computational cost. The maximum acceptable feature extraction computation time for a $256 \times 256$ image was set to 10 s to enable implementation of the cell segmentation algorithm on an ordinary personal computer. The recognition rates of standard deviation, mean by standard deviation, texture measure A, and kurtosis for cell segmentation on PLL glass using the $3 \times 3$ window size were close. After doing pairwise comparisons of these features on multiple images, kurtosis feature using $3 \times 3$ moving window size was found to be the most discriminative. For PLL glass, GLCM features were not required and were not used due to their high computational cost. For nanofibrillar scaffolds, the first two features of SFS result: power spectrum and standard deviation were used. The recognition rate of power spectrum plus standard deviation proved better than power spectrum alone for nanofibrillar scaffolds, and the computational cost of adding the standard deviation was low. For cell segmentation on Aclar and PLL Aclar surfaces, the feature set found by SFS using 5x5 moving window size was used. Window size increases were carefully investigated for cells on PLL Aclar surfaces; however, use of up to the $9 \times 9$ window size did not increase the cell segmentation recognition rate. Therefore, the feature set found by SFS using the $5 \times 5$ moving window size was also used for cells on PLL Aclar surfaces. Feature extraction computation times for $256 \times 256$ images via $3 \times 3$, $5 \times 5$, and $7 \times 7$ moving window sizes are compared in Figure 3. The final window size and feature set performance results for cell segmentation are summarized in Table 2. Representative examples of input AFM height and deflection images and cell segmentation results are shown in Figure 4. The low recognition rate for cell segmentation on PLL Aclar surfaces can be seen in the figure.

### Comparison of Conventional and New CSI Analysis Results

The conventional and the new CSIs were used to perform quantitative investigations of astrocyte responses as a function of 1) changes in nanophysical environment cues, and 2) dBcAMP-treatment. At 24 h, quiescent-like and reactive-like astrocytes on all substrates exhibited significant variation in their morphologies. The conventional CSI results, shown in Figure 5a, indicated that quiescent-like astrocytes cultured on

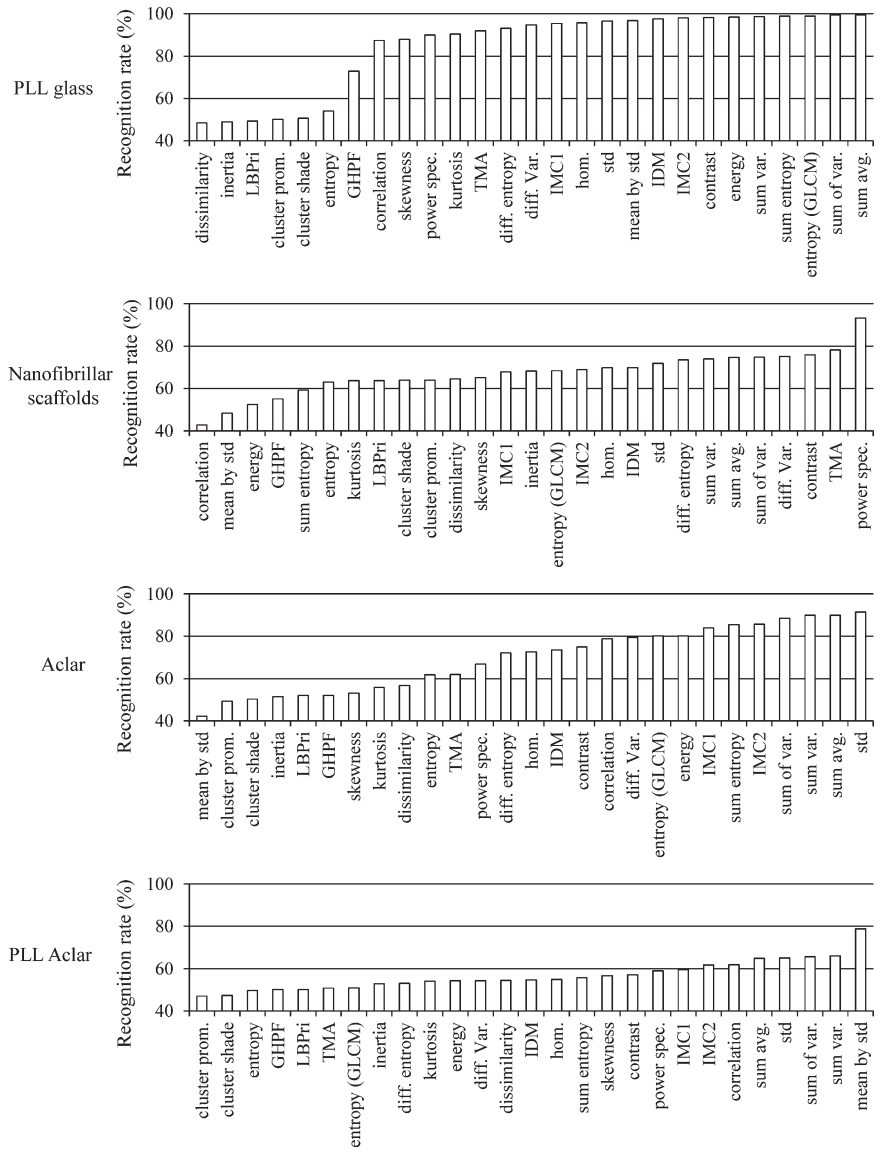


**Figure 2.** Recognition rates of individual texture features extracted from AFM height images using 5 × 5 moving window size. (std: standard deviation; GHPF: Gaussian high pass filter; TMA: texture measure A; spec: spectrum; LBPri: rotationally invariant local binary pattern; hom: homogeneity; IDM: inverse difference moment; avg: average; var: variance; diff: difference; IMC: information measure of correlation; cluster prom.: cluster prominence).

Aclar surfaces were more stellate than the ones on other surfaces. The mean CSI of astrocytes cultured on PLL Aclar and nanofibrillar scaffolds were close. The biomedical interpretation of the conventional CSI results would be that astrocytes cultured on nanofibrillar scaffolds and PLL Aclar were responsive to the dBcAMP-treatment whereas ones on Aclar and PLL Aclar were almost unchanged.

However, the new CSI results (Figure 5b) showed that both quiescent-like and reactive-like astrocytes cultured on the Aclar surfaces had the lowest mean CSI values. This implies that, with the same stellation counted in the new CSI, there is also dominant minimal spreading behavior. The new CSI analysis indicated that astrocytes cultured on Aclar surfaces were less spread than the ones on other substrates, and this is consistent with our previous independent AFM cross-section analysis (3). For all surfaces, the new CSI value was significantly increased after dBcAMP-treatment except the ones on PLL glass. The highest new CSI values were observed for quiescent-like astrocytes on PLL glass and reactive-like astrocytes on PLL Aclar. The new CSI of both the quiescent-like and reactive-like astrocytes on nanofibrillar scaffolds were in the midway between Aclar and PLL Aclar. The new CSI of quiescent-like and reactive-like astrocytes on PLL Aclar surfaces was significantly higher than the corresponding ones on Aclar surfaces. The biomedical interpretation of the new CSI values for astrocytes on PLL functionalized surfaces would be that PLL functionalization induced an increase in cell spreading for both quiescent-like and reactive-like astrocytes. This is

**Table 1.** SFS and SFFS algorithm results for AFM cell segmentation using different moving window sizes

| MOVING WINDOW SIZE | ACLAR | PLL ACLAR | NANOFIBRILLAR SCAFFOLDS | PLL GLASS |
|---|---|---|---|---|
| 3 × 3 | Standard deviation (h); power spectrum (h); power spectrum (d); [GLCM sum average (h)] | Mean by standard deviation (h); power spectrum (h); GLCM IMC 1 (d) | Standard deviation (d); power spectrum (h); entropy (h); mean by standard deviation (d) | GLCM correlation (h) standard deviation (d) |
| Recognition rate | 86.07% [86.56%] | 72.99% | 93.06% | 98.22% |
| 5 × 5 | standard deviation (h) | mean by standard deviation (h); mean by standard deviation (d) | power spectrum (h); standard deviation (d); mean by standard deviation (d) | GLCM sum average (h) |
| Recognition rate | 91.41% | 79.57% | 96.28% | 99.5% |
| 7 × 7 | GLCM sum of variances (h) GLCM IMC 2 (d) | mean by standard deviation (h); mean by standard deviation (d); GLCM energy (h) | power spectrum (h); power spectrum (d) | GLCM sum of variances (h) |
| Recognition rate | 94.09% | 81.79% | 97.29% | 99.77% |

Features found by SFS but SFFS are shown in square brackets. AFM source image is indicated by (h) for height and (d) for deflection. Features are listed in the order they were added to the feature subset. (IMC: information measure of correlation).

consistent both with our previous independent AFM cross-section analysis (3) and with the known interaction of positively charged PLL with negatively charged cell membrane moieties (40,41).

## Discussion

The present work is one of the first studies to explore the sub-optimal textural feature set for cell–scaffold/substrate segmentation of AFM cell culture images. As demonstrated by the present work, use of a feature set found by SFS and SFFS, enables cell segmentation in comparative situations with average recognition rate higher than 90%. This is a valuable approach for studies in which the biomedical goal is to investigate changes in cell behavior in response to varying environments, including variations in regenerative, stem cell, and cancer cell environments. In the present work, a feature set selected from 27 textural features including GLCM and local statistical models and a multi-layer neural network classifier were used to develop a semiautomatic cell segmentation algorithm for a comparative study of neural cells in four different regenerative environments. SFS and SFFS feature selection algorithms were implemented and identified an individual texture feature set for cell segmentation in the culture environments. The feature set selections were then further revised to meet a 10 s computational cost requirement for a 256 × 256 AFM image, enabling code access by a majority of users.[1]

In this work, a new CSI was defined that revealed quantitative cell spreading information not included in a conventional cell shape index. This required mathematical segmentation of cells from scaffolds/substrates. The difficulty of segmentation varied, depending on the textural similarity between cell membranes and substrate/scaffold surfaces. The surface roughness of a cell membrane has a large variance because of the different types of glycoproteins, cell protrusions, channels, and protein assemblies present. In terms of surface roughness, astrocyte cell membranes and PLL Aclar surfaces were closer than those of PLL glass and Aclar surfaces, resulting in a low recognition rate on PLL Aclar surfaces. The segmentation was also challenging on nanofibrillar scaffolds. Cells on nanofibrillar scaffolds interact with these surfaces via nanoscale edges and processes that are not distinguishable from the nanofibrillar background by AFM height or deflection (or phase, not shown) imaging. This is because the cellular edges and processes are approximately the same order in height as the background nanofibers, ∼100 to ∼300 nm. This difficulty was partly overcome by using GHPF as described in detail in Ref. 26.

The development of the new CSI in the present work was motivated by the need to accommodate obvious differences in cell spreading observed in response to regenerative environment differences, identified by the 3D volumetric capability of AFM imaging.

All cells need to attach to a native or synthetic extracellular matrix or to another cell to survive. The attachments may be relatively permanent, e.g., cardiomyocytes in heart tissue or dynamic, e.g., astrocyte perivascular endfeet in contact with capillary basement membranes at the blood–brain barrier. Cell spreading is a consequence of cell and surface interactions that are initiated with cell attachment (42). Figure 5b of our present work showed that the reactive-like astrocyte spreading on all culture surfaces, except PLL glass, were significantly higher than quiescent-like astrocyte spreading. This result indicates that cell spreading could be an indication of astrocyte immunoreactivity in culture.

[1]Codes are publically available at http://www.msu.egr.edu/ebnl

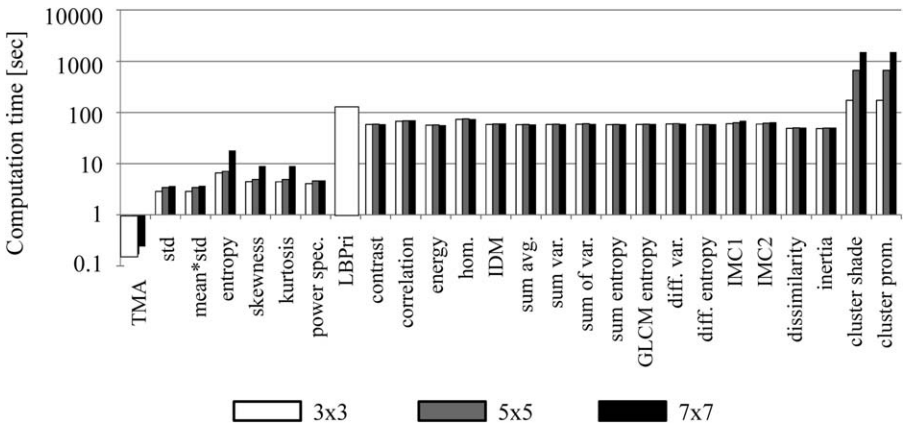


**Figure 3.** Feature extraction computation time for 256 × 256 images via 3 × 3, 5 × 5, and 7 × 7 moving window sizes. TMA, std, mean*std, and power spec. extraction time does not strongly depend on the moving window size whereas entropy, skewness, and kurtosis computation time increase as moving window size increase. GLCM textural feature extraction is computationally more expensive than local statistics except LBPri. GLCM feature extraction times do not depend on the window size and feature type except for cluster shade and cluster prominence. (std: standard deviation; TMA: texture measure A; spec: spectrum; LBPri: rotationally invariant local binary pattern; hom: homogeneity; IDM: inverse difference moment; avg: average; var: variance; diff: difference; IMC: information measure of correlation; cluster prom.: cluster prominence).

Cell spreading is related to how cell volume is distributed on a surface. If cell volume is mainly aggregated in the center and cell shape is like a hemisphere, then the cell is unspread. If cell volume is distributed evenly and cell has a flattened shape, then the cell is spread. A conventional CSI ignores the 3D shape of the cell, and uses only cell perimeter and cell projection area data from 2D images to represent the 2D shape of the cell. The new CSI analysis results in a combined measure of cell spreading and stellation information, thus utilizes the volumetric information provided by AFM. The calculation of the new CSI is practical since only cell surface area and cell volume measurements are required. The new CSI is, therefore, a new promising quantitative cell morphology evaluation method that is expected to be useful for biomedical research in regenerative medicine.

Use of the new CSI in the present work enabled quantitative results capable of biomedical interpretation. Our studies showed that the dBcAMP-treatment induced a statistically significant increase in the new CSI of cerebral cortical astrocytes for all surfaces except the ones on PLL glass. The unusual astrocyte response on PLL glass is possibly due to the high substrate stiffness (4). The new CSI of quiescent-like astrocytes on PLL glass was significantly higher than for other substrates. The high CSI for PLL glass indicated that astrocytes spread more on PLL glass than on other substrates, which is consistent with previously published results (43,44). Increased spreading with dBcAMP-treatment on Aclar, PLL Aclar, and nanofibrillar scaffolds, is possibly because the increased GFAP expression in astrocyte cytoskeleton induced spreading of astrocytes. The quiescent and reactive-like astrocytes on Aclar were less spread compared to the corresponding ones on PLL Aclar, which indicates that PLL functionalization induced cells to become more spread. The new CSI of astrocytes on nanofibrillar scaffolds was in the midway between Aclar and PLL functionalized surfaces indicating a moderate cell behavior on these surfaces. The quiescent-like astrocyte process thickness was higher than reactive-like astrocyte process thickness on nanofibrillar scaffolds, which is consistent with the increased spreading behavior with dBcAMP-treatment.

The important information about the cell spreading behavior was missing from the conventional CSI analysis. It is crucial to realize that the biomedical interpretation of the conventional CSI results, that astrocytes cultured on nanofibrillar scaffolds and PLL Aclar were responsive to the dBcAMP-treatment whereas ones on Aclar and PLL Aclar were almost unchanged, was incorrect and misleading.

The new CSI in the present work was developed for use with cells in culture. Recently, cell culture standard practice

**Table 2.** Texture feature sets proposed for AFM cell segmentation by considering both the recognition rate and the computational cost

| CULTURE SURFACE | ACLAR | PLL ACLAR | NANOFIBRILLAR SCAFFOLDS | PLL GLASS |
|---|---|---|---|---|
| Texture feature type | Standard deviation (h) | mean by standard deviation (h) (d) | power spectrum (h) standard deviation (d) | kurtosis (h) |
| Window size | 5 × 5 | 5 × 5 | 5 × 5 | 3 × 3 |
| Recognition rate | 91.41% | 79.57% | 95.56% | 96.78% |
| Average computation time (s) | 4.39 | 8.37 | 9.72 | 5.68 |

Average computation time is given for 20 randomly selected 256 × 256 pixel AFM images. The texture features extracted from AFM height and deflection images were indicated by (h) and (d), respectively.

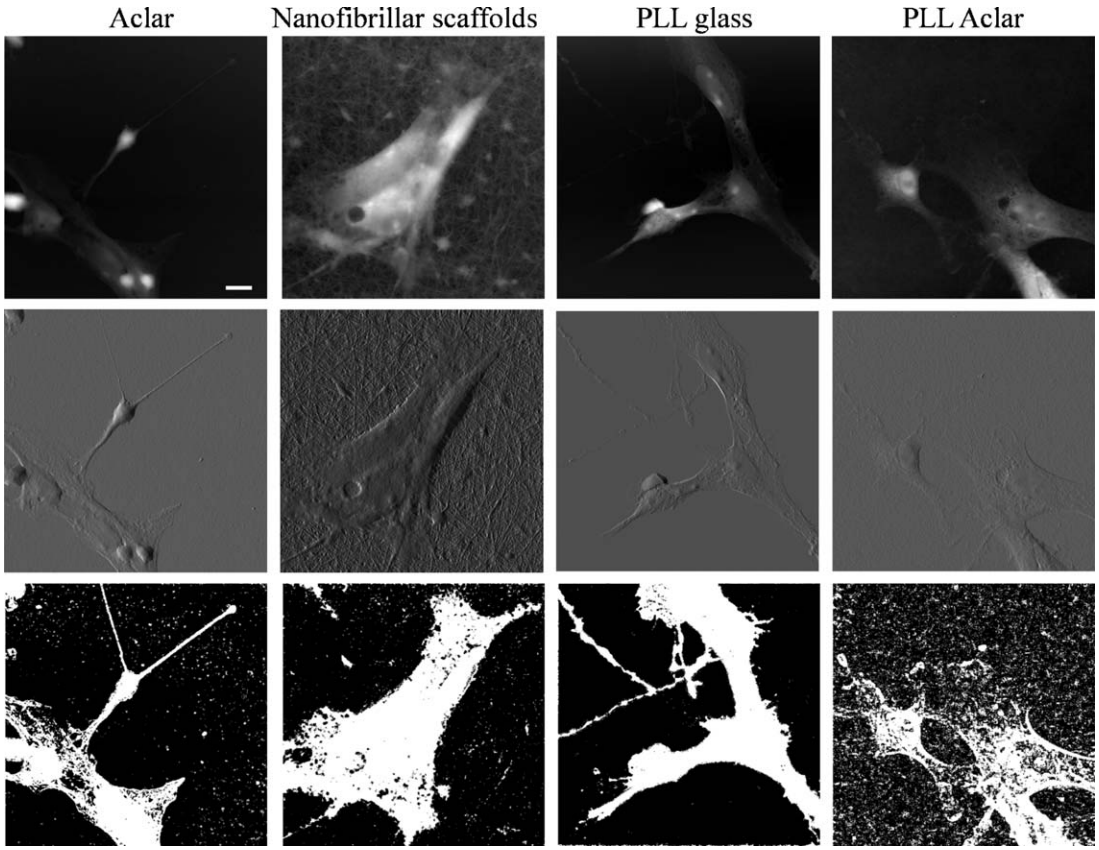


**Figure 4.** Cell segmentation results for AFM images of astrocytes cultured on Aclar, nanofibrillar scaffolds, PLL glass, and PLL Aclar. Top row: AFM height images; middle row: AFM deflection images; bottom row: segmentation results. White and black pixels represent cell and substrate/scaffold region found by neural network classifier, respectively. Scale bar, 10 $\mu$m.

has changed from using planar glass or plastic substrates to using fibrous and scaffold environments that produce more biomimetic cell morphology results. These changes in cell culture protocols result in cell segmentation texture changes, and therefore advantage in using our strategy of selection from a texture feature set.

Cells in culture are often investigated using optical techniques including confocal laser scanning microscopy (CLSM) (10,13) and recently superresolution microscopy (SR) in stochastic (PALM, STORM) and optical (STED) formats (45). AFM is relatively a novel instrument in the biomedical community (4,14). Its key advantage for use in quantitative CSI studies is its extremely high axial resolution, $<1$ nm in the z direction. Axial resolution for CLSM and also for stochastic SR is $\sim$200–500 nm, while axial resolution for optical SR can reach $\sim$50 nm through splitting its resolving light into two light paths. Total internal reflection fluorescence microscopy (TIRF) is another optical technique, which is used for specifically for its axial resolution, $\sim$100–200 nm (46). For cell volume analysis by any of these optical microscopy techniques, special stains that delineate the plasma membrane and have minimal intracellular diffusion must be used. Their fluorescence must also be compatible with all excitation and probe laser wavelengths, which require careful planning and execution of sample preparation. Furthermore, immunostaining

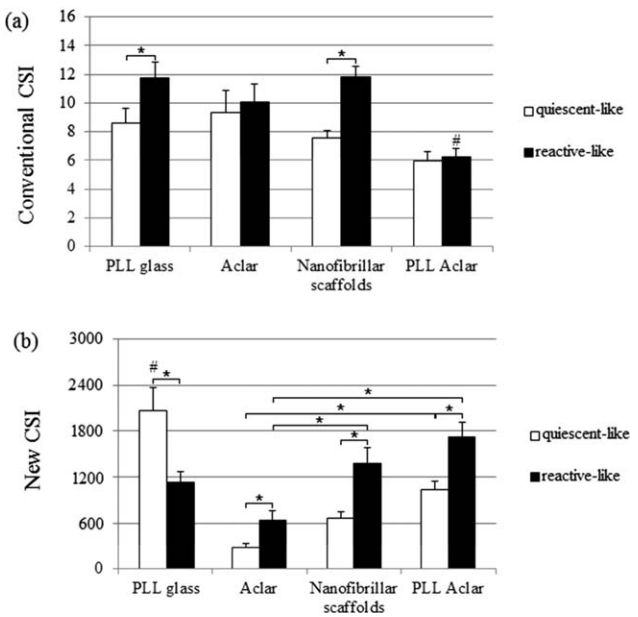


**Figure 5.** Average (**a**) conventional and (**b**) new cell shape index results for quiescent-like and reactive-like astrocytes. Error bars show SE of $n = 50$ astrocytes. * denotes significance, $P < 0.05$; # denotes significance from the same type of reactivity group, $P < 0.05$.

requires permeabilization of the cell membrane, which can significantly affect the cell spreading. AFM sample preparation is relatively easy, and it requires no staining, fixing, or labeling. Therefore, the cell volume and cell surface area calculations and hence the new CSI calculations from AFM images are the most accurate that are currently available and have the greatest integrity and ease of sample preparation. Because AFM is a surface technique, it cannot be used to characterize the cell spreading of cells cultured in 3D scaffolds or hydrogels. However, new techniques designed to combine the advantages of AFM with those of continuously improving optical microscopies are emerging (47). These techniques, coupled with powerful image processing analyses and interpretations, will lead to key advances in cell morphometry and to significant nanobiomedical discoveries.

## Acknowledgment

The authors declare that there are no conflicts of interest.

## Literature Cited

1. Matsutani S, Yamamoto N. Neuronal regulation of astrocyte morphology in vitro is mediated by GABAergic signaling. Glia 1997;20:1–9.
2. Vartanian KB, Kirkpatrick SJ, Hanson SR, Hinds MT. Endothelial cell cytoskeletal alignment independent of fluid shear stress on micropatterned surfaces. Biochem Biophys Res Commun 2008;371:787–792.
3. Tiryaki VM, Ayres VM, Khan AA, Ahmed I, Shreiber DI, Meiners S. Nanofibrillar scaffolds induce preferential activation of Rho GTPases in cerebral cortical astrocytes. Int J Nanomed 2012;7:3891–3905.
4. Tiryaki VM, Ayres VM, Ahmed I, Shreiber DI. Differentiation of reactive-like astrocytes cultured on nanofibrillar and comparative culture surfaces. Nanomedicine 2015;10:529–545.
5. Dike LE, Chen CS, Mrksich M, Tien J, Whitesides GM, Ingber DE. Geometric control of switching between growth, apoptosis, and differentiation during angiogenesis using micropatterned substrates. In Vitro Cell Dev Biol Anim 1999;35:441–448.
6. Chen CS, Mrksich M, Huang S, Whitesides GM, Ingber DE. Micropatterned surfaces for control of cell shape, position, and function. Biotechnol Prog 1998;14:356–363.
7. Chen CS, Mrksich M, Huang S, Whitesides GM, Ingber DE. Geometric control of cell life and death. Science 1997;276:1425–1428.
8. Canham PB, Burton AC. Distribution of size and shape in populations of normal human red cells. Circ Res 1968;22:405–422.
9. Bribiesca E. An easy measure of compactness for 2D and 3D shapes. Pattern Recognit 2008;41:543–554.
10. Chvátal A, Andrová M, Kirchhoff F. Three-dimensional confocal morphometry—A new approach for studying dynamic changes in cell morphology in brain slices. J Anat 2007;210:671–683.
11. Kassimi MA, Beqqali OE. 3D model retrieval based on semantic and shape indexes. Int J Comp Sci 2011;8:1–7.
12. Thibault G, Fertil B, Sequeira J, Mari J-L. Shape and texture indexes. Application to cell nuclei classification. Int J Pattern Recognit Artif Intell 2013;27:1–23.
13. Farooque TM, Camp CH, Tison CK, Kumar G, Parekh SH, Simon CG. Measuring stem cell dimensionality in tissue scaffolds. Biomaterials 2014;35:2558–2567.
14. Pincus Z, Theriot A. Comparison of quantitative methods for cell-shape analysis. J Microsc 2007;227:140–156.
15. Tiryaki VM, Adia-Nimuva U, Hartz SA, Xie K, Ayres VM, Ahmed I, Shreiber DI. New atomic force microscopy based astrocyte cell shape index. In: Rafailovich M, editor. MRS Online Proceedings Library. Boston, MA: Cambridge University Press; 2012. pp 1527.
16. Kouwer PH, Koepf M, Le Sage VA, Jaspers M, van Buul AM, Eksteen-Akeroyd ZH, Woltinge T, Schwartz E, Kitto HJ, Hoogenboom R, Picken SJ, Nolte RJ, Mendes E, Rowan AE. Responsive biomimetic networks from polyisocyanopeptide hydrogels. Nature 2013;493:651–655.
17. Marturano JE, Arena JD, Schiller ZA, Georgakoudi I, Kuo CK. Characterization of mechanical and biochemical properties of developing embryonic tendon. Proc Natl Acad Sci USA 2013;110:6370–6375.
18. Stewart MP, Helenius J, Toyoda Y, Ramanathan SP, Muller DJ, Hyman AA. Hydrostatic pressure and the actomyosin cortex drive mitotic cell rounding. Nature 2011; 469:226–230.
19. Kodera N, Yamamoto D, Ishikawa R, Ando T. Video imaging of walking myosin V by high speed atomic force microscopy. Nature 2010;468:72–76.
20. Meiners S, Ahmed I, Ponery AS, Amor N, Ayres VM, Fan Y, Chen Q, Babu AN. Engineering electrospun nanofibrillar surfaces for spinal cord repair: A discussion. Polym Int 2007;56:1340–1348.
21. Meiners S, Harris SL, Delgado-Rivera R, Ahmed I, Babu AN, Patel RP, Crockett DP. A nanofibrillar prosthetic modified with fibroblast growth factor-2 for spinal cord repair. In: Chang WN, editor. Nanofibers: Fabrication, Performance, and Applications. Hauppage, NY: Nova Science Publishers; 2009. pp 327–343.
22. Binnig G, Quate CF, Gerber C. Atomic force microscope. Phys Rev Lett 1986;56:930–933.
23. Eaton P, West P. Atomic Force Microscopy: AFM Modes. New York: Oxford University Press; 2010. pp 49–81.
24. Pudil P, Novovicova J, Kittler J. Floating search methods in feature selection. Pattern Recognit Lett 1994;15:1119–1125.
25. Bellman RE. Dynamic Programming. Princeton: Princeton University Press; 1957.
26. Tiryaki VM, Khan AA, Ayres VM. AFM feature definition for neural cells on nanofibrillar tissue scaffolds. Scanning 2012;34:316–324.
27. Bolle RM, Connell J, Haas N, Mohan R, Taubin G. Veggievision: A produce recognition system. In: Proceedings of the 3rd IEEE Workshop on Applications of Computer Vision. Sarasota, FL: IEEE; 1996. pp 244–251.
28. Leon-Garcia A. Probability and Random Processes for Electrical Engineering. Reading, MA: Addison-Wesley Publishing Company; 1994. 162 p.
29. Frigo M, Johnson SG. FFTW: An adaptive software architecture for the FFT. In: Proceedings of the International Conference on Acoustics, Speech, and Signal Processing, Vol. 3. Seattle, WA: IEEE; 1998. pp 1381–1384.
30. Ojala T, Pietikäinen M, Harwood D. A comparative study of texture measures with classification based on feature distributions. Pattern Recognit 1996;29:51–59.
31. Ojala T, Pietikäinen M, Mäenpää T. Multiresolution gray-scale and rotation invariant texture classification with local binary patterns. IEEE Trans Pattern Anal Mach Intell 2002;24:971–987.
32. Haralick RM, Shanmugam K, Dinstein I. Textural features for image classification. IEEE Trans Syst Man Cybern 1973;3:610–621.
33. Miyamoto E, Merryman JT. Fast calculation of Haralick texture features. Available at: http://users.ece.cmu.edu/~pueschel/teaching/18-799B-CMU-spring05/material/eizan-tad.pdf. Accessed on 3 March 2015.
34. Ciresan DC, Meier U, Schmidhuber J. Multi-column deep neural networks for image classification. In: IEEE Conference on Computer Vision and Pattern Recognition. Providence, RI: IEEE; 2012. pp 3642–3649.
35. Ciresan DC, Giusti A, Gambardella LM, Schmidhuber J. Deep Neural Networks Segment Neuronal Membranes in Electron Microscopy Images. Lake Tahoe, NV: NIPS; 2012. pp 2852–2860.
36. Riedmiller M, Braun H. A direct adaptive method for faster backpropagation learning: The RPROP algorithm. In: Proceedings of the IEEE International Conference on Neural Networks. San Fransisco, CA: IEEE; 1993. pp 586–591.
37. Duda RO, Hart PE, Stork DG. Pattern Classification, 2nd ed. New York, NY: Wiley; 2000. 282 p.
38. MathWorks Support Team. How can I calculate the area of my surface plot in MATLAB 7.9 (R2009b)? Available at: http://www.mathworks.com/matlabcentral/answers/93117-how-can-i-calculate-the-area-of-my-surface-plot-in-matlab-7-9-r2009b Accessed on 16 June 2015.
39. Korchev YE, Gorelik J, Lab MJ, Sviderskaya EV, Johnston CL, Coombes CR, Vodyanoy I, Edwards CRW. Cell volume measurement using scanning ion conductance microscopy. Biophys J 2000;78:451–457.
40. Cook GMW. Glycoproteins in membranes. Biol Rev 1968;43:363–391.
41. Finkelstein EI, Chao PG, Hung CT, Bulinski JC. Electric field-induced polarization of charged cell surface proteins does not determine the direction of galvanotaxis. Cell Motility Cytoskeleton 2007;64:833–846.
42. Fardin MA, Rossier OM, Rangamani P, Avigan PD, Gauthier NC, Vonnegut W, Mathur A, Hone J, Iyengar R, Sheetz MP. Cell spreading as a hydrodynamic process. Soft Matter 2010;6:4788–4799.
43. Georges PC, Miller WJ, Meaney DF, Sawyer ES, Janmey PA. Matrices with compliance comparable to that of brain tissue select neuronal over glial growth in mixed cortical cultures. Biophys J 2006;90:3012–3018.
44. Moshayedi P, Costa LF, Christ A, Lacour SL, Fawcett J, Guck J, Franze K. Mechanosensitivity of astrocytes on optimized polyacrylamide gels analyzed by quantitative morphometry. J Phys Condens Matter 2010;22:194114.
45. Betzig E, Hell SW, Moerner WE. Jointly awarded the Nobel Prize for chemistry "for the development of super-resolved fluorescence microscopy," 2014 Available at: www.nobelprize.org/nobel_prizes/chemistry/laureates/2014/
46. Spira F, Dominguez-Escobar J, Müller N, Wedlich-Söldner R. Visualization of cortex organization and dynamics in microorganisms, using total internal reflection fluorescence microscopy. J Vis Exps 2012;63:1–7.
47. Chacko JV, Harke B, Canale C, Diaspro A. Cellular level nanomanipulation using atomic force microscope aided with superresolution imaging. J Biomed Opt 2014;19: 105003.